Biomedical Optics EXPRESS

Erythrocyte-derived nano-probes functionalized with antibodies for targeted near infrared fluorescence imaging of cancer cells

Jenny T. Mac,[1] Vicente Nuñez,[2] Joshua M. Burns,[2] Yadir A. Guerrero,[2] Valentine I. Vullev,[1,2] and Bahman Anvari[1,2,*]

[1]*Department of Biochemistry, University of California Riverside, 900 University Ave., Riverside, CA 92521, USA*
[2]*Department of Bioengineering, University of California, Riverside, 900 University Ave., Riverside, CA 92521, USA*
[*]*anvarib@ucr.edu*

Abstract: Constructs derived from mammalian cells are emerging as a new generation of nano-scale platforms for clinical imaging applications. Herein, we report successful engineering of hybrid nano-structures composed of erythrocyte-derived membranes doped with FDA-approved near infrared (NIR) chromophore, indocyanine green (ICG), and surface-functionalized with antibodies to achieve molecular targeting. We demonstrate that these constructs can be used for targeted imaging of cancer cells *in vitro*. These erythrocyte-derived optical nano-probes may provide a potential platform for clinical translation, and enable molecular imaging of cancer biomarkers.

OCIS codes: (170.2520) Fluorescence microscopy; (110.3080) Infrared imaging; (160.4236) Nanomaterials; (160.1435) Biomaterials; (170.3880) Medical and biological imaging.

References and links

1. J. V. Frangioni, "In vivo near-infrared fluorescence imaging," Curr. Opin. Chem. Biol. **7**(5), 626–634 (2003).
2. W. F. Cheong, S. A. Prahl, and A. J. Welch, "A Review of the Optical-Properties of Biological Tissues," IEEE J. Quantum Electron. **26**(12), 2166–2185 (1990).
3. S. A. Hilderbrand, K. A. Kelly, M. Niedre, and R. Weissleder, "Near infrared fluorescence-based bacteriophage particles for ratiometric pH imaging," Bioconjug. Chem. **19**(8), 1635–1639 (2008).
4. L. A. Yannuzzi, "Indocyanine Green Angiography: A Perspective On Use In The Clinical Setting," Am. J. Ophthalmol. **151**(5), 745–751 (2011).
5. C. Hirche, D. Murawa, Z. Mohr, S. Kneif, and M. Hünerbein, "ICG fluorescence-guided sentinel node biopsy for axillary nodal staging in breast cancer," Breast Cancer Res. Treat. **121**(2), 373–378 (2010).
6. E. M. Sevick-Muraca, R. Sharma, J. C. Rasmussen, M. V. Marshall, J. A. Wendt, H. Q. Pham, E. Bonefas, J. P. Houston, L. Sampath, K. E. Adams, D. K. Blanchard, R. E. Fisher, S. B. Chiang, R. Elledge, and M. E. Mawad, "Imaging of lymph flow in breast cancer patients after microdose administration of a near-infrared fluorophore: feasibility study," Radiology **246**(3), 734–741 (2008).
7. L. M. Crane, G. Themelis, H. J. Arts, K. T. Buddingh, A. H. Brouwers, V. Ntziachristos, G. M. van Dam, and A. G. van der Zee, "Intraoperative near-infrared fluorescence imaging for sentinel lymph node detection in vulvar cancer: first clinical results," Gynecol. Oncol. **120**(2), 291–295 (2011).
8. J. R. van der Vorst, B. E. Schaafsma, F. P. Verbeek, R. J. Swijnenburg, M. Hutteman, G. J. Liefers, C. J. van de Velde, J. V. Frangioni, and A. L. Vahrmeijer, "Dose optimization for near-infrared fluorescence sentinel lymph node mapping in patients with melanoma," Br. J. Dermatol. **168**(1), 93–98 (2013).
9. S. Jeschke, L. Lusuardi, A. Myatt, S. Hruby, C. Pirich, and G. Janetschek, "Visualisation of the lymph node pathway in real time by laparoscopic radioisotope- and fluorescence-guided sentinel lymph node dissection in prostate cancer staging," Urology **80**(5), 1080–1087 (2012).
10. H. A. Zaidi, A. A. Abla, P. Nakaji, S. A. Chowdhry, F. C. Albuquerque, and R. F. Spetzler, "Indocyanine green angiography in the surgical management of cerebral arteriovenous malformations: lessons learned in 130 consecutive cases," Neurosurgery **10Suppl 2**, 246–251 (2014).
11. K. Roessler, M. Krawagna, A. Dörfler, M. Buchfelder, and O. Ganslandt, "Essentials in intraoperative indocyanine green videoangiography assessment for intracranial aneurysm surgery: conclusions from 295 consecutively clipped aneurysms and review of the literature," Neurosurg. Focus **36**(2), E7 (2014).
12. J. C. Kraft and R. J. Ho, "Interactions of indocyanine green and lipid in enhancing near-infrared fluorescence properties: the basis for near-infrared imaging in vivo," Biochemistry **53**(8), 1275–1283 (2014).
13. T. Toyota, H. Fujito, A. Suganami, T. Ouchi, A. Ooishi, A. Aoki, K. Onoue, Y. Muraki, T. Madono, M. Fujinami, Y. Tamura, and H. Hayashi, "Near-infrared-fluorescence imaging of lymph nodes by using liposomally formulated indocyanine green derivatives," Bioorg. Med. Chem. **22**(2), 721–727 (2014).

#257163 Received 11 Jan 2016; revised 2 Mar 2016; accepted 10 Mar 2016; published 16 Mar 2016

14. L. Wu, S. Fang, S. Shi, J. Deng, B. Liu, and L. Cai, "Hybrid polypeptide micelles loading indocyanine green for tumor imaging and photothermal effect study," Biomacromolecules **14**(9), 3027–3033 (2013).
15. M. A. Yaseen, J. Yu, M. S. Wong, and B. Anvari, "Stability assessment of indocyanine green within dextran-coated mesocapsules by absorbance spectroscopy," J. Biomed. Opt. **12**(6), 064031 (2007).
16. M. Kester, Y. Heakal, T. Fox, A. Sharma, G. P. Robertson, T. T. Morgan, E. I. Altinoğlu, A. Tabaković, M. R. Parette, S. M. Rouse, V. Ruiz-Velasco, and J. H. Adair, "Calcium phosphate nanocomposite particles for in vitro imaging and encapsulated chemotherapeutic drug delivery to cancer cells," Nano Lett. **8**(12), 4116–4121 (2008).
17. P. Sharma, N. E. Bengtsson, G. A. Walter, H. B. Sohn, G. Zhou, N. Iwakuma, H. Zeng, S. R. Grobmyer, E. W. Scott, and B. M. Moudgil, "Gadolinium-doped silica nanoparticles encapsulating indocyanine green for near infrared and magnetic resonance imaging," Small **8**(18), 2856–2868 (2012).
18. G. Kim, S. W. Huang, K. C. Day, M. O'Donnell, R. R. Agayan, M. A. Day, R. Kopelman, and S. Ashkenazi, "Indocyanine-green-embedded PEBBLEs as a contrast agent for photoacoustic imaging," J. Biomed. Opt. **12**(4), 044020 (2007).
19. B. Bahmani, C. Y. Lytle, A. M. Walker, S. Gupta, V. I. Vullev, and B. Anvari, "Effects of nanoencapsulation and PEGylation on biodistribution of indocyanine green in healthy mice: quantitative fluorescence imaging and analysis of organs," Int. J. Nanomedicine **8**, 1609–1620 (2013).
20. C. Gutiérrez Millán, C. I. Colino Gandarillas, M. L. Sayalero Marinero, and J. M. Lanao, "Cell-based drug-delivery platforms," Ther. Deliv. **3**(1), 25–41 (2012).
21. A. Antonelli and M. Magnani, "Red blood cells as carriers of iron oxide-based contrast agents for diagnostic applications," J. Biomed. Nanotechnol. **10**(9), 1732–1750 (2014).
22. V. Agrawal, J. H. Woo, G. Borthakur, H. Kantarjian, and A. E. Frankel, "Red blood cell-encapsulated L-asparaginase: potential therapy of patients with asparagine synthetase deficient acute myeloid leukemia," Protein Pept. Lett. **20**(4), 392–402 (2013).
23. C. M. Hu, R. H. Fang, and L. Zhang, "Erythrocyte-inspired delivery systems," Adv. Healthc. Mater. **1**(5), 537–547 (2012).
24. V. R. Muzykantov, "Drug delivery by red blood cells: vascular carriers designed by mother nature," Expert Opin. Drug Deliv. **7**(4), 403–427 (2010).
25. J. W. Yoo, D. J. Irvine, D. E. Discher, and S. Mitragotri, "Bio-inspired, bioengineered and biomimetic drug delivery carriers," Nat. Rev. Drug Discov. **10**(7), 521–535 (2011).
26. A. A. Bentley and J. C. Adams, "The Evolution Of Thrombospondins And Their Ligand-Binding Activities," Mol. Biol. Evol. **27**(9), 2187–2197 (2010).
27. P. A. Oldenborg, A. Zheleznyak, Y. F. Fang, C. F. Lagenaur, H. D. Gresham, and F. P. Lindberg, "Role of CD47 as a marker of self on red blood cells," Science **288**(5473), 2051–2054 (2000).
28. P. A. Oldenborg, "CD47: A Cell Surface Glycoprotein Which Regulates Multiple Functions of Hematopoietic Cells in Health and Disease," ISRN Hematol. **2013**, 614619 (2013).
29. P. L. Rodriguez, T. Harada, D. A. Christian, D. A. Pantano, R. K. Tsai, and D. E. Discher, "Minimal "Self" Peptides That Inhibit Phagocytic Clearance And Enhance Delivery Of Nanoparticles," Science **339**(6122), 971–975 (2013).
30. B. Bahmani, D. Bacon, and B. Anvari, "Erythrocyte-derived photo-theranostic agents: hybrid nano-vesicles containing indocyanine green for near infrared imaging and therapeutic applications," Sci. Rep. **3**, 2180 (2013).
31. M. Yan, B. A. Parker, R. Schwab, and R. Kurzrock, "HER2 aberrations in cancer: implications for therapy," Cancer Treat. Rev. **40**(6), 770–780 (2014).
32. D. P. English, D. M. Roque, and A. D. Santin, "HER2 expression beyond breast cancer: therapeutic implications for gynecologic malignancies," Mol. Diagn. Ther. **17**(2), 85–99 (2013).
33. R. H. Fang, C. M. Hu, K. N. Chen, B. T. Luk, C. W. Carpenter, W. Gao, S. Li, D. E. Zhang, W. Lu, and L. Zhang, "Lipid-insertion enables targeting functionalization of erythrocyte membrane-cloaked nanoparticles," Nanoscale **5**(19), 8884–8888 (2013).
34. J. P. Delord, C. Allal, M. Canal, E. Mery, P. Rochaix, I. Hennebelle, A. Pradines, E. Chatelut, R. Bugat, S. Guichard, and P. Canal, "Selective inhibition of HER2 inhibits AKT signal transduction and prolongs disease-free survival in a micrometastasis model of ovarian carcinoma," Ann. Oncol. **16**(12), 1889–1897 (2005).
35. V. Tolmachev, H. Wallberg, M. Sandström, M. Hansson, A. Wennborg, and A. Orlova, "Optimal specific radioactivity of anti-HER2 Affibody molecules enables discrimination between xenografts with high and low HER2 expression levels," Eur. J. Nucl. Med. Mol. Imaging **38**(3), 531–539 (2011).
36. B. S. Jung, V. I. Vullev, and B. Anvari, "Revisiting Indocyanine Green: Effects of serum and physiological temperature on absorption and fluorescence characteristics," IEEE J. Sel. Top. Quantum Electron. **20,** 7000409 (2014).
37. D. Mahl, C. Greulich, W. Meyer-Zaika, M. Koller, and M. Epple, "Gold nanoparticles: dispersibility in biological media and cell-biological effect," J. Mater. Chem. **20**(29), 6176–6181 (2010).
38. Z. E. Allouni, M. R. Cimpan, P. J. Høl, T. Skodvin, and N. R. Gjerdet, "Agglomeration and sedimentation of TiO2 nanoparticles in cell culture medium," Colloids Surf. B Biointerfaces **68**(1), 83–87 (2009).
39. T. Tadros, "Steric Stabilization," in *Encyclopedia of Colloid and Interface Science*, T. Tadros, ed. (Springer Berlin Heidelberg, Berlin, Heidelberg, 2013), pp. 1048–1049.
40. S. Kittler, C. Greulich, J. S. Gebauer, J. Diendorf, L. Treuel, L. Ruiz, J. M. Gonzalez-Calbet, M. Vallet-Regi, R. Zellner, M. Koller, and M. Epple, "The influence of proteins on the dispersability and cell-biological activity of silver nanoparticles," J. Mater. Chem. **20**(3), 512–518 (2010).
41. R. Flower, E. Peiretti, M. Magnani, L. Rossi, S. Serafini, Z. Gryczynski, and I. Gryczynski, "Observation of Erythrocyte Dynamics in the Retinal Capillaries and Choriocapillaris Using ICG-Loaded Erythrocyte Ghost Cells," Invest. Ophthalmol. Vis. Sci. **49**(12), 5510–5516 (2008).

#257163 Received 11 Jan 2016; revised 2 Mar 2016; accepted 10 Mar 2016; published 16 Mar 2016

42. C. M. J. Hu, L. Zhang, S. Aryal, C. Cheung, R. H. Fang, and L. Zhang, "Erythrocyte membrane-camouflaged polymeric nanoparticles as a biomimetic delivery platform," Proc. Natl. Acad. Sci. U.S.A. **108**(27), 10980–10985 (2011).
43. J. Rahmer, A. Antonelli, C. Sfara, B. Tiemann, B. Gleich, M. Magnani, J. Weizenecker, and J. Borgert, "Nanoparticle encapsulation in red blood cells enables blood-pool magnetic particle imaging hours after injection," Phys. Med. Biol. **58**(12), 3965–3977 (2013).
44. B. E. Bax, M. D. Bain, P. J. Talbot, E. J. Parker-Williams, and R. A. Chalmers, "Survival of human carrier erythrocytes in vivo," Clin. Sci. **96**(2), 171–178 (1999).
45. F. Bossa, A. Latiano, L. Rossi, M. Magnani, O. Palmieri, B. Dallapiccola, S. Serafini, G. Damonte, E. De Santo, A. Andriulli, and V. Annese, "Erythrocyte-Mediated Delivery Of Dexamethasone in Patients With Mild-to-Moderate Ulcerative Colitis, Refractory to Mesalamine: A Randomized, Controlled Study," Am. J. Gastroenterol. **103**(10), 2509–2516 (2008).
46. L. Rao, L. L. Bu, J. H. Xu, B. Cai, G. T. Yu, X. Yu, Z. He, Q. Huang, A. Li, S. S. Guo, W. F. Zhang, W. Liu, Z. J. Sun, H. Wang, T. H. Wang, and X. Z. Zhao, "Red Blood Cell Membrane as a Biomimetic Nanocoating for Prolonged Circulation Time and Reduced Accelerated Blood Clearance," Small **11**(46), 6225–6236 (2015).
47. J. Shi, Z. Xiao, N. Kamaly, and O. C. Farokhzad, "Self-Assembled Targeted Nanoparticles: Evolution of Technologies and Bench to Bedside Translation," Acc. Chem. Res. **44**(10), 1123–1134 (2011).
48. N. Kamaly, Z. Xiao, P. M. Valencia, A. F. Radovic-Moreno, and O. C. Farokhzad, "Targeted polymeric therapeutic nanoparticles: design, development and clinical translation," Chem. Soc. Rev. **41**(7), 2971–3010 (2012).
49. D. Peer, J. M. Karp, S. Hong, O. C. Farokhzad, R. Margalit, and R. Langer, "Nanocarriers as an emerging platform for cancer therapy," Nat. Nanotechnol. **2**(12), 751–760 (2007).

1. Introduction

Fluorescence imaging using near infrared (NIR) wavelengths, particularly in the 700-1450 nm spectral range, continues to be an important imaging modality in clinical and biomedical applications. There are two key advantages in using NIR wavelengths. First, the NIR "transparency window" facilitates relatively deep penetration of light, on the order of 2-3 cm, due to the reduced absorption of photons by water and proteins, as well as the diminished scattering within the NIR spectral band [1–3]. Second, given that there is minimal auto-fluorescence in NIR spectral bands, the use of an exogenous fluorescent probe enhances the image contrast.

Intraoperative NIR fluorescence imaging has gained entry into clinical studies [1]. By combining NIR fluorescent probes with molecular targeting agents, the specificity of such probes can be enhanced. One particular NIR exogenous chromophore is indocyanine green (ICG). To-date, ICG remains the only NIR dye approved by the United States Food and Drug Administration (FDA) for specific imaging applications, and one of the least toxic agents administered to humans [1]. In addition to its current clinical imaging usage for specific indications such as choroidal circulation [4], ICG has been investigated for sentinel lymph node mapping in patients with various types of cancer [5–9], and imaging of intracranial aneurysm and cerebral arteriovenous malformations [10, 11].

Despite its use in such medical applications, the major drawbacks of ICG include its non-specificity, and short half-life within plasma (≈2-4 min). Encapsulation into nano-sized structures has been investigated as an approach to shield ICG from non-specific interactions with plasma proteins, and extend its circulation time. To-date, ICG has been encapsulated into various nano-sized constructs including those composed of micelles, liposomes, synthetic polymers [12–15], calcium phosphate [16], and silica and silicate matrices [17, 18]. We have previously reported on encapsulation of ICG into polymeric nanoparticles, coated with poly ethylene glycol (PEG), as a technique to increase the blood circulation time of ICG and delay its hepatic accumulation for up to an hour [19].

Mammalian cells such as erythrocytes, lymphocytes, and macrophages are receiving increased attention as new types of platforms for the delivery of therapeutic or imaging agents [20–25]. A particular feature of normal erythrocytes that distinguishes them from other cell types is their naturally long circulation time (≈90-120 days), attributed to the presence of "self-marker" proteins on their surface to inhibit immune response [23, 25]. One putative self-marker is CD47 glycoprotein [26, 27], which impedes phagocytosis through signaling with the phagocyte receptor, SIRPα (CD172a) [28, 29]. Therefore, a key potential advantage of

#257163 Received 11 Jan 2016; revised 2 Mar 2016; accepted 10 Mar 2016; published 16 Mar 2016

erythrocytes as a delivery platform is that by making their cargo (e.g. ICG) available over a long time, imaging may be performed over an extended time.

Our group recently reported the first successful engineering of nano-sized structures derived from erythrocytes doped with ICG, and their utility as light-activated theranostic agents for fluorescence imaging and photothermal destruction of human cells [30]. We refer to these constructs as NIR erythrocyte-derived transducers (NETs). Expanding on our previous work, in this paper we report for the first time the successful functionalization of the NETs surface with antibodies as molecular recognition biomolecules, and demonstrate the utility of antibody-functionalized NET as nano-probes for specific NIR fluorescence imaging of cancer cells *in vitro*.

2. Materials and methods

2.1. NETs fabrication and functionalization with antibodies

Erythrocytes were separated from bovine whole blood (Rockland Immunochemicals, Inc., Limerick, PA) by centrifugation (1000 × *g*, 5 min, 4°C). Plasma and the buffy coat were discarded, and the resulting packed erythrocytes were washed three times in 1x (≈320 mOsm) phosphate buffer saline (PBS). Packed erythrocytes were then subject to hypotonic treatment (1 ml of 0.25x PBS (≈80 mOsm), pH = 8, 5 min, 4°C), after which they were centrifuged (20,000 × *g*, 15 min, 4°C). The supernatant was discarded. Hypotonic treatment of erythrocytes in 0.25x PBS, and centrifugation was repeated until hemoglobin was removed, resulting in an opaque white pellet. The pellet was resuspended in 1 ml of 1x PBS. Upon completion of this step, hemoglobin-depleted micron-sized erythrocyte ghosts (EGs) were obtained.

To demonstrate proof-of-principle, we chose antibodies against the human epidermal growth receptor (HER2) as the test antibody to functionalize the NETs. HER2 is a clinically important receptor biomarker involved in carcinogenesis of various solid tumors, particularly breast, colorectal, non-small cell lung cancer, and ovarian cancer [31, 32]. Nevertheless, our approach can be readily used to functionalize the NETs with other antibodies.

The functionalization process was as follows and shown in Fig. 1. First, we activated the aldehyde functional groups on anti-HER2 (30 µg) (Santa Cruz Biotechnology, Inc., Dallas, TX) using oxidation with sodium periodate (10 µl of 100 mM) (Sigma Aldrich, St. Louis, MO). Excess oxidizing agent was removed by filtering the activated anti-HER2 through 50k Amicon Ultra-4 centrifuge filter units (Millipore, Temecula, CA). Next, to covalently attach the activated anti-HER2 to the NETs surface, we used a linker molecule, 1,2-distearoyl-sn-glycero-3-phosphoethanolamine - polyethylene glycol - amine (DSPE-PEG-NH_2) (2000 Da) (Nanocs, Inc, New York, NY), connected to the surface of EGs through lipid insertion in water followed by filtration and exchange of buffer to 1x PBS through 50k Amicon Ultra-4 centrifuge filter units. A similar lipid insertion method of a linker molecule has been reported for functionalization of erythrocyte membrane-cloaked polymeric nanoparticles [33].

We then extruded the EGs bearing lipid-inserted DSPE-PEG-NH_2, and suspended in 1 ml of 1x PBS containing 100 µM of ICG, 20 times through 400 nm polycarbonate porous membranes followed by 20 additional extrusions through 100 nm diameter membranes using an Avanti mini extruder (Avanti Polar Lipids, Inc., Alabaster, Al). This step results in loading of ICG into the EGs to form NETs. NETs bearing lipid-inserted DSPE-PEG-NH_2 were mixed with activated anti-HER2 for five minutes, and then incubated with 5 µl of 20 mM sodium dithionite, as the reducing agent, for 30 minutes at 4 °C to finally produce NETs functionalized with anti-HER2. Excess reducing agent was removed, and anti-HER2 functionalized NETs were isolated through ultra-centrifugation (≈53,000 × *g*, 1 hour, 4°C). The supernatant was discarded. The pellet was washed three times, and re-suspended in 1 ml of 1x PBS, and stored in the dark at 4 °C. The procedure for fabrication of non-functionalized NETs was similar as above except that EGs without any additional surface modification were suspended in 1 ml of 1x PBS containing 100 µM of ICG, and extruded.

#257163 Received 11 Jan 2016; revised 2 Mar 2016; accepted 10 Mar 2016; published 16 Mar 2016

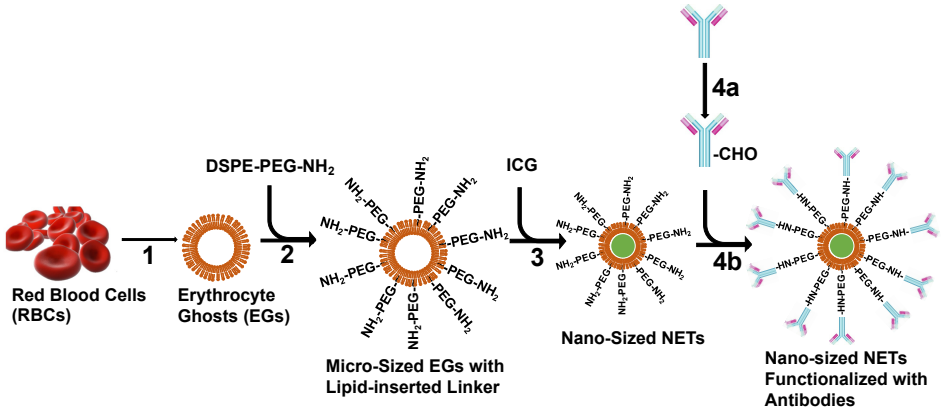

Fig. 1. Schematic of the methodology to fabricate NETs functionalized with antibodies. The various steps are defined as follows: (1) hemoglobin depletion; (2) lipid insertion of linker molecule DSPE-PEG-NH_2; (3) sequential extrusion through 400 nm and 100 nm porous membranes, and ICG loading; (4a) antibody oxidation to activate the aldehyde groups; and (4b) antibody conjugation by reductive amination.

2.2 NETs characterization

The hydrodynamic diameters of non-functionalized and anti-HER2 functionalized NETs were determined by dynamic light scattering (DLS) (Zetasizer Nanoseries, NanoZS90, Malvern Instruments, Malvern, UK). The absorption spectra of non-functionalized and anti-HER2 functionalized NETs were obtained using a UV Visible spectrophotometer (Cary 50 UV-Vis spectrophotometer, Agilent Technologies, Santa Clara, CA) with optical path length of 1 cm. The fluorescence spectra of non-functionalized and anti-HER2 functionalized NETs were acquired in response to photo-excitation at 650 nm excitation with a 450W xenon lamp, and recorded using a fluorometer (Fluorolog-3 spectrofluorometer, Edison, NJ).

To prepare samples for scanning electron microscopy (SEM) imaging, samples were fixed with 2.5% glutaraldehyde, overnight. Then, 10 µl of sample was added to poly-L-lysine coated slide for 5 minutes, dried (Critical-point-dryer Balzers CPD0202), sputter coated with platinum, and imaged with SEM FEI NNS450. To confirm successful antibody-functionalization, non-functionalized NETs (control) and anti-HER2 functionalized NETs were incubated with fluorescein isothiocyanate (FITC)-labeled secondary rabbit antibody (30 µg) (Life Technologies, Carlsbad, CA) for one hour. Excess secondary antibody was filtered through 100k Amicon Ultra-4 centrifuge filter. The FITC fluorescence spectra were acquired in response to photo-excitation at 488 nm with a 450W xenon lamp, and recorded using the fluorometer.

2.3 Aggregation assessment

To assess possible aggregation of the NETs, particularly after functionalization, both non-functionalized and functionalized NETs were pelleted and re-suspended in 1 ml of either 1x PBS, Rosewell Park Memorial Institute (RPMI) 1640 cell culture medium (Mediatech, Inc, Manassas, VA), or RPMI 1640 supplemented with 10% fetal bovine serum (FBS) (Thermo Fisher Scientific, Waltham, MA). The hydrodynamic diameter distributions were obtained by DLS within 1-2 hours of incubation of the particles with each of the three dispersion agents.

2.4 Assessment of NETs absorption stability

We used micron-sized (non-extruded) EGs to fabricate non-functionalized NETs. EGs were incubated with hypotonic buffer (Na_2HPO_4/ $Na_2H_2PO_4$, 140 mOsm, pH 5.8), and ICG dissolved in water so that the ICG concentration in this loading solvent was 50 µM. Suspensions were then incubated for five minutes at 4 °C in dark, centrifuged at 20,000 × *g* for 15 minutes, and washed twice with 1x PBS to remove any non-encapsulated ICG. The

#257163 Received 11 Jan 2016; revised 2 Mar 2016; accepted 10 Mar 2016; published 16 Mar 2016

resulting micron-sized NETs were re-suspended in cold 1x PBS buffer solution. We obtained the absorption spectra of the NETs suspended in 1 ml of 1x PBS immediately after fabrication (Day 0), and at every other day post-fabrication for up to 8 days.

2.5 Assessment of CD47 presence on NETs

To access for the presence of CD47 on the surface of NETs, we incubated non-extruded (micron-sized) EGs (positive control), and non-functionalized nano-sized NETs fabricated after extrusion of the EGs (as described in section 2.1) with FITC-labeled anti-CD47 (4 μg) (Santa Cruz Biotechnology, Inc, Dallas, TX) for one hour at 4 °C. As the negative control sample, we used Texas Red-labeled liposomes (which lack CD47), and incubated them with FITC-labeled anti-CD47 in a similar manner as those used for incubation of EGs and NETs. Excess and unbound antibody were removed by centrifugation (≈53,000 × *g*, 1 hour, 4°C). Fluorescence emission spectra of all samples were acquired in response to photo-excitation at 488 nm with a 450W xenon lamp, and recorded using the fluorometer.

2.6 Targeted fluorescence imaging of cancer cells

To validate the effectiveness of anti-HER2 functionalized NETs in targeting the HER2 receptors, we used two types of human epithelial ovarian cancer cells, SKOV3 and OVCAR3, which have relatively high and low HER2 expression levels, respectively [34, 35]. We added 100 μl of SKOV3 or OVCAR3 cell suspension (≈10^6 cells/ml) in RPMI 1640 medium supplemented with 1% Penicillin/Streptomycin, and 10% FBS (ATCC, Manassas, VA) to each well of a 96-well flat bottom micro-titer plate. Cell suspensions were plated in 5% CO_2 overnight. On the following day, the old culture medium was replaced with fresh medium. We incubated the cells at 37 °C with 100 μl of 1x PBS (negative control), ≈9 μM free ICG (negative control), non-functionalized (positive control), or anti-HER2 functionalized NET, in separate wells for two hours in the dark. Cells were subsequently washed twice with 1x PBS, and finally incubated with 4',6-diamidino-2-phenylindole (DAPI) for 15 minutes to stain the nuclei for fluorescence imaging.

NIR fluorescence emission (> 770 nm) in response to 740 ± 35 nm excitation by a Nikon halogen lamp was captured by an electron multiplier gained CCD camera (Quant EM-CCD, C9100-14 Hamamatsu, Shizuoka-ken, Japan). The camera exposure time was set at 0.7 s. Fluorescence emission from DAPI in the range of 435–485 nm was collected in response to 360 ± 20 nm excitation by a Nikon halogen lamp. We present falsely colored microscopic fluorescent images as the overlay of the NIR emission due to ICG (red channel), and visible emission due to DAPI-stained nuclei (blue channel).

3. Results and discussion

3.1 Characterization of NETs

In Fig. 2(a), we present the diameter distributions for populations of non-functionalized and anti-HER2 functionalized NETs, as determined by the DLS technique. The estimated mean peak diameter of non-functionalized NETs was ≈162 nm with full width at half maximum (FWHM) diameter value of ≈85 nm. Upon functionalization with anti-HER2, the mean peak diameter increased to ≈252 nm, suggesting that the thickness of the DSPE-PEG-NH_2 linker and the antibody grafted onto the NETs was ≈45 nm. The FWHM diameter value for population of anti-HER2-functionalized NETs increased to ≈225 nm, suggesting possible aggregation among the particles.

We present an SEM image of anti-HER2 functionalized NETs in Fig. 2(b). As demonstrated by this image, the morphology of the anti-HER2 functionalized NETs was nearly spherical, and the diameter values were consistent with those as determined by the DLS technique.

#257163 Received 11 Jan 2016; revised 2 Mar 2016; accepted 10 Mar 2016; published 16 Mar 2016

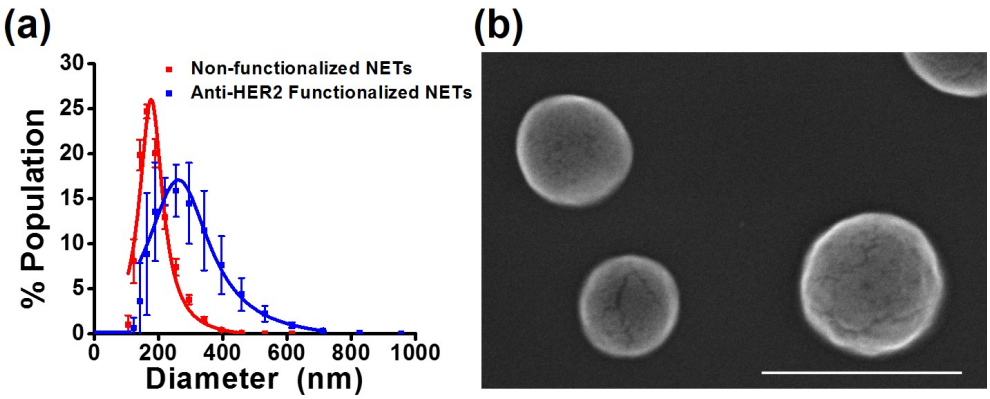

Fig. 2. (a) Diameter distributions of non-functionalized, and anti-HER2 functionalized NETs as determined by dynamic light scattering. We present the mean of three measurements on each of the samples with error bars representing the standard deviations from the mean. We fitted Lorentzian functions to the measured diameter distributions (solid curves). (b) Illustrative SEM image of anti-HER2 functionalized NETs. Scale bar = 500 nm.

We validated the functionalization of NETs using a secondary antibody labeled with FITC. As show in Fig. 3(a), the fluorescence emission spectrum of the NETs bearing the primary anti-HER2 and the secondary antibody showed a spectral peak at 520 nm, associated with FITC, in response to photo-excitation at 488 nm, confirming the successful grafting of anti-HER2 onto the NETs.

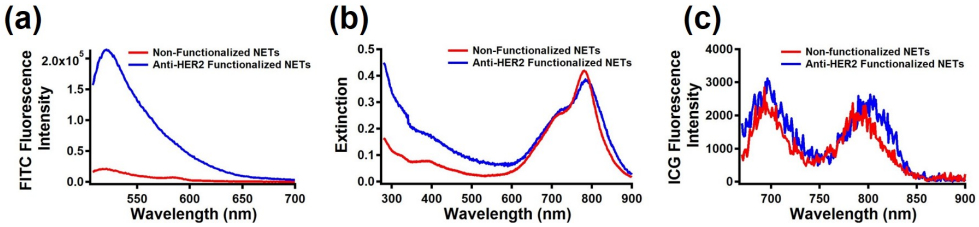

Fig. 3. (a) Fluorescence emission spectra of non-functionalized NETs, and NETs functionalized with primary and FITC-labeled secondary antibodies. Photo-excitation wavelength was 488 nm, and fluorescence emissions > 508 nm were recorded. (b) Extinction spectra of non-functionalized, and anti-HER2 functionalized NETs. (c) Fluorescence emission spectra of non-functionalized and anti-HER2 functionalized NETs. Photo-excitation wavelength was 650 nm, and fluorescence emissions > 665 nm were recorded.

In Fig. 2(b), we present the extinction spectra, resulting from the combined effects of absorption and scattering, for non-functionalized and anti-HER2 functionalized NETs. The spectra in the 650-900 nm range were nearly identical, and attributed to the presence of ICG. Specifically, spectral peaks at ≈735 nm and 795 nm are associated with absorption by H-like aggregate and monomeric forms of ICG, respectively [36]. The value at 280 nm is predominantly associated with the absorption of membrane proteins on NETs, and increased from ≈0.16 for non-functionalized NETs to ≈0.45 for anti-HER2 functionalized NETs. We attribute this increase to the presence of the antibodies successfully grafted onto the NETs. The overall increase in the extinction values associated with anti-HER2 functionalized NETs up to 600 nm is likely due to increased scattering by these particles, resulting from both an increase in diameter at the individual particle level after functionalization as well as possible aggregation among some of the particles. As demonstrated in Fig. 3(c), the fluorescence emission spectrum of anti-HER2 functionalized NETs resembled that of the non-functionalized NETs, indicating that functionalization did not alter the emission characteristics of the NETs. In response to photo-excitation at 650 nm, there were spectral

#257163 Received 11 Jan 2016; revised 2 Mar 2016; accepted 10 Mar 2016; published 16 Mar 2016

peaks at ≈700 and 798 nm, which correspond to the H-like aggregate and monomeric forms of ICG, respectively.

3.2 Aggregation assessment

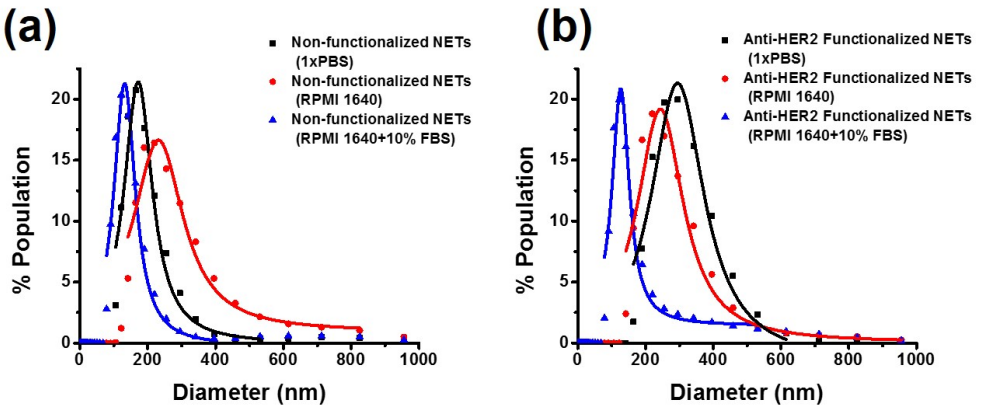

Fig. 4. Hydrodynamic diameter distributions for (a) non-functionalized, and (b) anti-HER2 functionalized NETs incubated in 1x PBS, RPMI 1640 cell culture medium, and RPMI 1640 + 10% FBS. Each symbol on the plots represents the average diameter value of three populations of either non-functionalized or anti-HER2 functionalized NETs. Measurements were fitted by Lorentzian functions (solid traces).

As evidenced by the results shown in Fig. 4(a), the mean peak diameter for these populations of non-functionalized NETs increased from ≈197 nm to ≈278 nm when changing the incubation medium from 1x PBS to RPMI 1640. The FWHM diameter value correspondingly increased from ≈98 nm to 187 nm. These increased values in peak and FWHM diameters are suggestive of the aggregation of non-functionalized NETs in RPMI 1640 cell culture medium. Similar aggregation effects have been reported for gold [37] and TiO_2 [38] nanoparticles when incubated in RPMI 1640 cell culture medium. The RPMI 1640 cell culture medium includes a variety of inorganic salts (e.g., sodium chloride, and sodium bicarbonate) in addition to various amino acids, vitamins, and glucose. The increased salt level reduces the electrostatic repulsion among the particles, leading to their aggregation [38]. When incubated in 10% FBS-supplemented RPMI 1640 cell culture medium, which is representative of physiological environment, the mean peak and FWHM diameter values were reduced to ≈157 nm and 74 nm, respectively, suggesting a reduction in aggregate fractions within the population. Adsorption of FBS proteins (predominantly albumin) on the surface of NETs can possibly lead to steric stabilization to produce strong repulsions among the particles, leading to reduced agglomerate content [38–40].

In Fig. 4(b), we present the diameter distribution profiles for anti-HER2 functionalized NETs incubated in 1x PBS, RPMI 1640 cell culture medium, or RPMI 1640 supplemented with 10% FBS. The mean peak diameter for these populations of anti-HER2 functionalized NETs was lowered from ≈307 nm to ≈272 nm when changing the incubation medium from 1x PBS to RPMI 1640. The FWHM diameter value correspondingly decreased from ≈176 nm to 167 nm. These decreased values in peak and FWHM diameters suggest that the presence of increased salt content within the RPMI 1640 cell culture medium was not sufficient to reduce electrostatic repulsions among the anti-HER2 functionalized NETs and cause further aggregation. However, when incubated in the physiologically-relevant medium of RPMI 1640 supplemented with 10% FBS, the peak and FWHM diameter values correspondingly decreased to ≈173 nm to 68 nm, indicating that there was considerable reduction in the aggregate fractions within the population of anti-HER2 functionalized NETs. Again, this

#257163 Received 11 Jan 2016; revised 2 Mar 2016; accepted 10 Mar 2016; published 16 Mar 2016

reduced agglomerate content may result from adsorption of FBS serum proteins (mainly albumin) on the surface of anti-HER2 functionalized NETs.

3.3 Absorption stability of NETs

As shown in Fig. 5, the absorption spectra of NETs remained nearly stable for at least 8 days post-fabrication. The absorbance value associated with the monomer form of ICG at 804 nm was reduced by only 5%, suggesting that this fraction of ICG may have leaked out over 8 days.

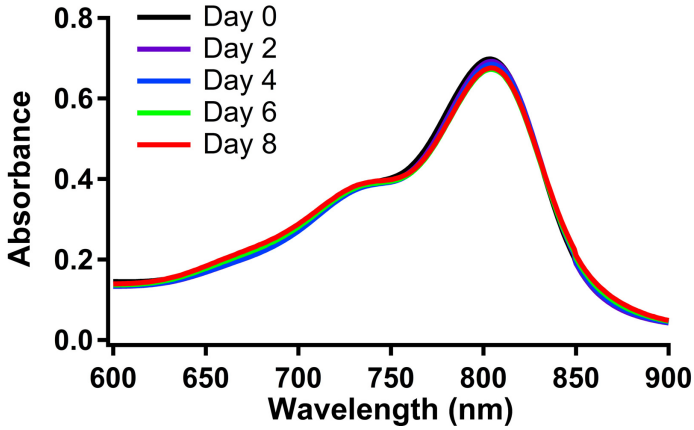

Fig. 5. Time-dependent absorption spectra of non-functionalized NETs post-fabrication.

3.4 Presence of CD47

In Fig. 6, we present the fluorescence emission spectra of micron-sized EGs (non-extruded) (positive control), nano-sized NETs (extruded) conjugated with FITC-labeled anti-CD47, and Texas Red-labeled liposomes (negative control). The presence of CD47 on both micron-sized (non-extruded) EGs and nano-sized NETs (formed after extruding the EGs) was confirmed by the fluorescence emission spectra, which showed spectral peaks associated with FITC at 520 nm. These results also suggest that the membranes on NETs remained as the right-side-out to accommodate anti-CD47 binding. The liposomes only showed an emission peak associated with Texas Red at 609 nm, indicating that they did not bind to anti-CD47.

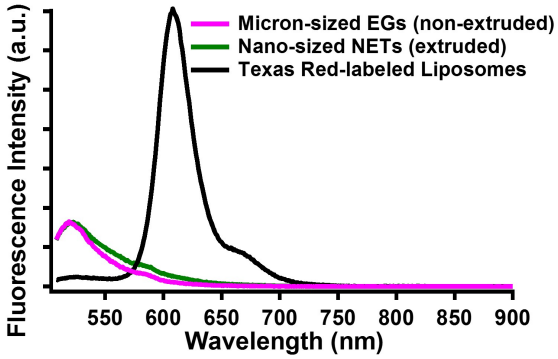

Fig. 6. Fluorescence emission spectra of micron-sized EGs (non-extruded) (positive control), nano-sized NETs (extruded) conjugated with FITC-labeled anti-CD47, and Texas Red-labeled liposomes (negative control). Emission spectra from EGs and NETs show FITC-associated spectral peaks at 520 nm (488 nm photo-excitation wavelength), indicating the presence of CD47. Liposomes exhibited an emission peak associated with Texas Red at 609 nm (488 nm photo-excitation wavelength).

#257163 Received 11 Jan 2016; revised 2 Mar 2016; accepted 10 Mar 2016; published 16 Mar 2016

3.5 Specific molecular targeting using functionalized NETs

We investigated the specific molecular targeting capability of functionalized NETs by fluorescence imaging of OVCAR3 and SKOV3 cancer cells, which have relatively low and high expression levels of the HER2 receptor. The overlay of the visible fluorescence emission due to DAPI (falsely colored in blue) and NIR emission due to ICG (falsely colored in red), corresponding to OVCAR3 and SKOV3 cells, are shown in Figs. 7(a) and 7(b), respectively. There was minimal NIR emission from OVCAR3 cells following two hours of incubation with anti-HER2 functionalized NETs at physiological temperature (37 °C). However, NIR emission from SKOV3 was detected after two hours of incubation with anti-HER2 functionalized NETs, indicating the effectiveness of these nano-constructs in targeting HER2. We quantified the fluorescence emission from the cell images by integrating the emission over the spectral band > 770 nm. Results of such quantification are shown in Fig. 7(c). The integrated NIR emission from SKOV3 cells was nearly 11 times higher than that from OVCAR3 cells, indicating the effectiveness of anti-HER2 functionalized in targeted fluorescence imaging of SKOV3 cells that have high over-expression of HER2 receptors.

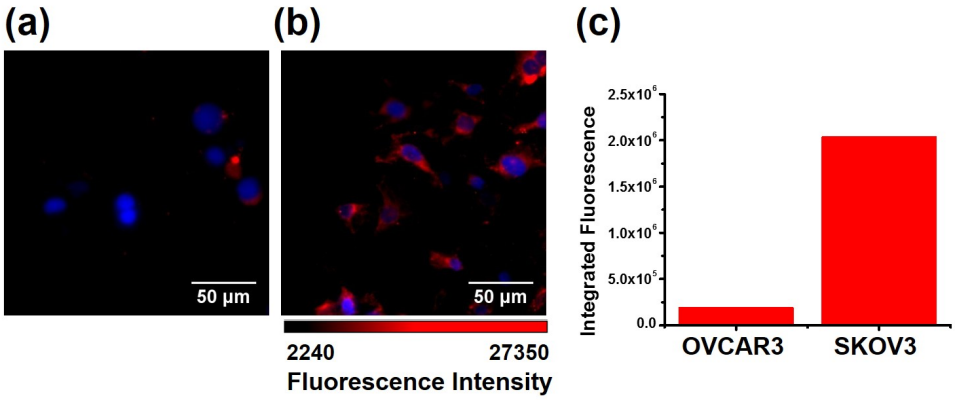

Fig. 7. Fluorescent images of (a) OVCAR3 cells (low HER2 expression), and (b) SKOV3 cells (high HER2 expression) following two hours of incubation at 37 °C with anti-HER2 functionalized NETs. Images are falsely colored. Blue channel: DAPI. Red channel: NIR emission due to ICG. (c) NIR fluorescence emission of images (a-b) integrated over the spectral band > 770 nm.

To further validate the specificity of anti-HER2 functionalized NETs in targeting the HER2 receptors, we incubated the SKOV3 cells with 1x PBS and free (non-encapsulated) ICG as negative controls, non-functionalized NETs (positive control), and anti-HER2 functionalized NETs for two hours at 37 °C. Results of these experiments are presented in Fig. 8. As shown in Figs. 8(a)-8(d), while there were none or minimal NIR emission from SKOV3 cells incubated with the control agents, NIR emission was detected from these cells following incubation with anti-HER2 functionalized NETs. NIR emission from these cell images was quantified as spectrally integrated emission values, and presented in Fig. 8(e), after subtracting the integrating emission from cells incubated in 1x PBS. The integrated NIR emission from SKOV3 cells incubated with anti-HER2 functionalized NETs was nearly 2.5 times higher than that of the SKOV3 cells incubated with non-functionalized NETs. The fluorescence emission from SKOV3 cells incubated with free ICG and non-functionalized NETs can be attributed to non-receptor mediated endocytosis. Anti-HER2 functionalized NETs undergo receptor-mediated endocytosis, and can be fluorescently imaged within the SKOV3 cells. These results confirm that specific targeting of HER2 receptors at physiological temperature can be achieved with anti-HER2 functionalized NETs, and demonstrate the potential of NETs equipped with molecular recognition biomolecules for targeted imaging of cancer cells.

#257163 Received 11 Jan 2016; revised 2 Mar 2016; accepted 10 Mar 2016; published 16 Mar 2016

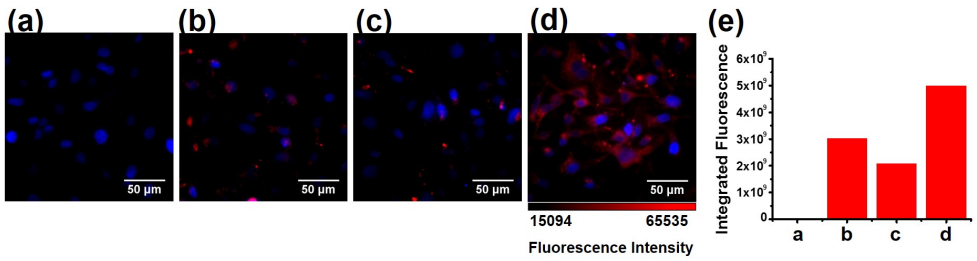

Fig. 8. Fluorescent images of SKOV3 cells following two hours of incubation at 37 °C with (a) 1x PBS, (b) free ICG, (c) non-functionalized NETs, and (d) anti-HER2 functionalized NETs. Images are falsely colored. Blue channel: DAPI. Red channel: NIR emission due to ICG. (e) NIR fluorescence emission of images (a-d) integrated over the spectral band >770 nm.

To the best of our knowledge, this is the first report of successful engineering of nano-sized optical vesicles derived from erythrocyte-derived and functionalized at the surface with antibodies for targeted NIR imaging of cancer cells. NETs offer several potential advantages: As constructs that can be engineered autologously, or from compatible blood types, NETs may potentially serve as non-immunogenic, and non-toxic platforms for optical imaging. In a previous *in vitro* study, we demonstrated human cells remained viable after incubation with NETs [30]. While the biocompatibility of NETs needs to be ultimately established, Flower et al. reported no immune or allergic responses, even after multiple injections of ICG-loaded human-derived EGs into monkeys and rabbits [41].

While the *in vivo* circulation kinetics of NETs has yet to be determined, Hu et al., reported that 80 nm diameter nano-constructs, composed of a poly (lactic-co-glycolic acid) core coated with erythrocyte-derived membranes, were retained in mice blood for three days with circulation half-life of nearly 40 hrs [42]. Rahmer et al. demonstrated that EGs loaded with superparamagnetic iron oxide nanoparticles were detectable in mice blood 24 hrs after tail vein injection [43]. A mean circulation half-life of 21.6 days has been reported for unloaded autologously-derived EGs in healthy humans [44]. Bossa et al. reported detectable levels of autologously-derived EGs containing dexamethasone in plasma of humans at 14 days post-infusion [45]. In a recent study, Rao et al. demonstrated that erythrocyte-membrane coated Fe_3O_4 nanoparticles were retaind in mice circulation at 48 hours post injection [46].

NETs are constructed easily at non-extreme temperatures (in the range of 4-25°C) without the use of any major chemical synthesis procedures. They are also are highly cost effective and fabricated without the need for expensive equipment. Currently, only a few liposomal drugs, none with targeting capability and none with imaging capability, have been approved by the FDA for different clinical applications [47]. Other presently non-FDA approved nano-based platforms are in various phases of clinical studies [48, 49], emphasizing the importance of such constructs in biomedicine. NETs provide a new class of optical nano-constructs, and may have widespread implications in medicine, particularly in relation to imaging of different cancer types. Moreover, NETs offer the potential to overcome the existing limitations of ICG (i.e., short half-life and lack of targeting ability). Given the existing FDA-approved status of ICG as well as humanized antibodies (e.g., Herceptin, Perjeta, and Kadcyla which target the HER2 receptor) antibody-functionalized NETs may provide an excellent platform for clinical translation.

The focus of this study has been to show that the NETs could be functionalized with antibodies as targeting moieties, and subsequently, demonstrate the proof-of-principle that such functionalized NETs could be used for targeted NIR imaging of cancer cells expressing particular receptors (e.g., HER2). For ultimate *in vivo* applications, further important studies are needed. In particular, the concentration of ICG utilized in fabrication of the NETs will need to be optimized in order to maximize the fluorescence emission of the NETs. Another important step in that direction is to determine the circulation kinetics and biodistribution of NETs. Finally, the effectiveness of functionalized NETs for cancer imaging will need to be

#257163 Received 11 Jan 2016; revised 2 Mar 2016; accepted 10 Mar 2016; published 16 Mar 2016

validated in animal models. We are currently pursuing such studies, and will be reporting the results as they become available.

4. Conclusion

We have demonstrated the successful engineering of erythrocyte-derived nanoparticles doped with ICG, and their surface functionalization with antibodies. Our experimental results demonstrate the effectiveness of NETs functionalized with anti-HER2 in targeted imaging of HER2 expressing cancer cells *in vitro*.

Acknowledgments

This work was supported in part by grants from the National Science Foundation (CBET-1509218), and University of California Cancer Research Coordinating Committee (5-44189-34912). Additional support was provided by the Office of Research and Economic Development at the University of California, Riverside (UCR). The electron microscopy images were obtained at the Central Facility for Advanced Microscopy and Microanalysis (CFAMM) at UCR. Texas Red-labeled liposomes were graciously provided by Soroush Ardekani from Dr. Kaustabh Ghosh's laboratory in the Department of Bioengineering at UCR.